



ELSEVIER

Ocean Modelling 4 (2002) 121–135

**Ocean
Modelling**

www.elsevier.com/locate/omodo1

The role of nonhydrostatic dynamics in controlling development of a surface ocean front

Thomas W.N. Haine ^{a,*}, Paul D. Williams ^b

^a *Department of Earth and Planetary Sciences, The Johns Hopkins University, 329 Olin Hall, Baltimore, MD 21218, USA*

^b *Atmospheric, Oceanic and Planetary Physics, University of Oxford, Oxford, UK*

Received 12 July 2001; received in revised form 24 August 2001; accepted 24 August 2001

Abstract

Numerical studies of surface ocean fronts forced by inhomogeneous buoyancy loss show nonhydrostatic convective plumes coexisting with baroclinic eddies. The character of the vertical overturning depends sensitively on the treatment of the vertical momentum equation in the model. It is less well known how the frontal evolution over scales of $O(10\text{ km})$ is affected by these dynamics. Here, we compare highly resolved numerical experiments using nonhydrostatic and hydrostatic models and the convective-adjustment parametrization. The impact of nonhydrostatic processes on average cross-frontal transfer is weak compared to the effect of the $O(1\text{ km})$ scale baroclinic motions. For water-mass distribution and formation rate nonhydrostatic dynamics have similar influence to the baroclinic eddies although adequate resolution of the gradients in forcing fluxes is more important. The overall implication is that including nonhydrostatic surface frontal dynamics in ocean general circulation models will have only a minor effect on scales of $O(1\text{ km})$ and greater. © 2002 Elsevier Science Ltd. All rights reserved.

Keywords: Oceanic fronts; Nonhydrostatic dynamics; Parametrization

1. Introduction

Open-ocean deep convection is the principal way in which mode-waters in the main thermoclines of mid-latitude gyres are ventilated. It is also an important process in the renewal of deep and abyssal waters at high latitudes. Despite its global significance for ocean circulation, deep convection is intermittent and geographically isolated. These facts have been known for several decades, but detailed knowledge of the controlling dynamics is only now emerging (Marshall and

* Corresponding author. Tel.: +1-410-516-7048; fax: +1-410-516-7933.

E-mail address: thomas.haine@jhu.edu (T.W.N. Haine).

Schott, 1999; The Lab Sea Group, 1998). Nonhydrostatic, inertial processes seem to be crucial for controlling convective plumes with scales up to $O(1 \text{ km})$. At larger scales, overturning plumes coexist and interact with fronts and eddies which are mainly hydrostatic and geostrophic. Yet quantitative understanding of this interaction has remained elusive.

Numerical models of the ocean circulation play a central role in understanding this interaction between convective motions and the ambient balanced flow. The concurrent simulation of this range of scales has only recently become feasible using models in idealized configurations. At the same time, realistic general circulation models (GCMs) of the basin-wide flow are now approaching horizontal resolutions comparable to the ocean depth and nonhydrostatic effects may thus become important. It is therefore now possible, and necessary, to study the importance of nonhydrostatic, convective dynamics on scales of $O(1\text{--}10 \text{ km})$ using numerical ocean models. Addressing this issue is our objective here.

The specific aim of this contribution is to investigate the importance of nonhydrostatic convection for frontal development averaged over $O(10 \text{ km})$. We use a highly resolved Navier–Stokes model to simultaneously capture nonhydrostatic gravitational overturning and baroclinic eddies. The underlying dynamical interactions are described in an earlier study (Haine and Marshall, 1998, hereafter HM98), which we now extend by comparing nonhydrostatic calculations with a hydrostatic simulation and a model including a convective adjustment scheme. Klinger et al. (1996) also studied the representation of convective plumes by vertical adjustment parametrization although in an open-ocean deep convection regime. Our quantitative assessment of the potential for nonhydrostatic motions to affect fronts provides guidance for GCM users who are considering including these dynamics in their models.

This paper is laid out as follows: First, we briefly review the nonhydrostatic primitive equations and scaling arguments that suggest when hydrostasy is a reliable assumption (Sections 2.1–2.3). Next, we describe the experimental set-up (Section 2.4). The results are in Section 3 and the discussion is in Section 4.

2. Dynamical models of the upper ocean

Here we briefly review the three models of upper ocean dynamics studied in this paper. They are the nonhydrostatic (NH) primitive equations, taken to represent the true fluid dynamics, and two approximate versions: the hydrostatic (HY) primitive equations and the hydrostatic primitive equations with a convective-adjustment (CA) parametrization.

2.1. The nonhydrostatic model

The *nonhydrostatic* equations governing the evolution of an incompressible, Boussinesq fluid on an f -plane are:

$$\frac{D\mathbf{v}_h}{Dt} + f\hat{\mathbf{k}} \times \mathbf{v}_h = -\frac{1}{\rho_{\text{ref}}} \nabla_h p + \left(v_h \nabla_h^2 + v_v \frac{\partial^2}{\partial z^2} \right) \mathbf{v}_h, \quad (1)$$

$$\frac{Dw}{Dt} = -\frac{1}{\rho} \frac{\partial p}{\partial z} - g + \left(v_h \nabla_h^2 + v_v \frac{\partial^2}{\partial z^2} \right) w, \quad (2)$$

$$\nabla_{\mathbf{h}} \cdot \mathbf{v}_{\mathbf{h}} + \frac{\partial w}{\partial z} = 0, \quad (3)$$

$$\rho = \rho_{\text{ref}} [1 - \alpha(T - T_{\text{ref}})], \quad (4)$$

$$\frac{DT}{Dt} = \frac{1}{c\rho_{\text{ref}}} \left(\kappa_{\mathbf{h}} \nabla_{\mathbf{h}}^2 T + \kappa_{\mathbf{v}} \frac{\partial^2 T}{\partial z^2} + \mathcal{H} \right). \quad (5)$$

The state variables are: $(\mathbf{v}_{\mathbf{h}}(\mathbf{r}, t), w(\mathbf{r}, t))$, $p(\mathbf{r}, t)$, $\rho(\mathbf{r}, t)$, and $T(\mathbf{r}, t)$ which represent the Cartesian velocity, pressure, density and temperature fields, respectively. This closed system comprises the Navier–Stokes equation (written in horizontal (subscript h) and vertical (subscript v) components, (1) and (2), with total derivative D/Dt), the incompressibility condition (3), a linearized equation of state of sea water in temperature only (4), and the heat energy conservation equation (5). There is a prescribed heat source $\mathcal{H}(\mathbf{r}, t)$ but no body forces driving the flow. The constants α and c are the thermal expansion coefficient and specific heat capacity at constant pressure of sea water and ν and κ are the kinematic viscosity and thermal diffusivity written with distinct horizontal and vertical components. The Coriolis parameter is f , g is the acceleration due to gravity downwards (negative \mathbf{k} direction), and T_{ref} is the temperature at which the density takes its Boussinesq value, ρ_{ref} . The boundary conditions are discussed in Section 2.4.

2.2. The hydrostatic model

We assume that the nonhydrostatic primitive equations can accurately represent the true evolution of the upper ocean over a range of scales ($O(10 \text{ m})$ – $O(10 \text{ km})$), at least for the present case. Under some circumstances, however, simpler dynamics apply. In particular, the vertical force balance is often close to *hydrostatic* balance. That is, the vertical acceleration Dw/Dt associated with a density anomaly $\delta\rho$ and pressure anomaly δp is small (it is strictly zero for exact hydrostatic balance). To see this point, write the (inviscid) vertical momentum equation (2) as

$$\frac{Dw}{Dt} = -\frac{1}{\rho} \frac{\partial \delta p}{\partial z} - \frac{g\delta\rho}{\rho} \quad (6)$$

($\delta\rho$ and δp are deviations from a hydrostatic, resting, background state). Scaling this equation reveals that Dw/Dt becomes progressively smaller, and the fluid more hydrostatic, as the nonhydrostatic parameter, n , vanishes. Marshall et al. (1997a) show that the dimensionless nonhydrostatic parameter is

$$n = \frac{\gamma^2}{Ri}, \quad (7)$$

where γ is the aspect ratio of the flow (vertical length scale divided by horizontal length scale) and Ri is the Richardson number.

So, for shallow fluids with strong stratification and weak vertical shear (small γ and large Ri) the pressure field is close to hydrostatic. In this case the vertical momentum equation is replaced by the diagnostic relation,

$$\frac{1}{\rho} \frac{\partial p}{\partial z} = -g, \quad (8)$$

and the vertical velocity field is found by vertically integrating the continuity relation (3). Marshall et al. (1997a,b) provide further details and numerical solution strategies for both the non-hydrostatic and hydrostatic systems. In particular, their nonhydrostatic pressure solvers span the transition from hydrostatic to nonhydrostatic flow without a large extra computational burden. Almost all ocean GCMs assume hydrostatic balance (8) applies a priori. In our hydrostatic experiment HY, we also make this assumption mindful that our model is not in a small n limit. We then compare results to experiment NH to identify the role of the nonhydrostatic dynamics.

2.3. The convective adjustment model

While hydrostatic balance applies almost universally in the ocean interior, isolated, intermittent nonhydrostatic motions play a crucial role in the general circulation. In an attempt to capture these effects most GCMs include a parametrization of their influence. Perhaps the most simple scheme is the convective adjustment algorithm (Cox, 1984; Marotzke, 1991). It acts to remove static instability by instantaneous vertical mixing. At each time-step the density field is examined to identify sites of unstable vertical density gradient and at those places the properties of vertically adjacent grid cells are combined. Typically, this process is repeated until all static instability has been erased. The convective adjustment scheme is implemented here in experiment CA which also assumes hydrostatic balance in the vertical momentum equation. The convective adjustment algorithm captures the essence of the gravitational overturning caused by surface ocean buoyancy loss in a computationally efficient way. It is therefore widely used in GCMs that cannot explicitly resolve these motions.

2.4. Experimental configuration

The experimental configuration is identical to that used by HM98 and only brief details are given here. The fluid is contained in a periodic channel of dimensions 50 km long, 30 km wide, and 2 km deep (Fig. 1). The vertical side walls and flat bottom are adiabatic and stress free and homogeneous Neumann pressure boundary conditions apply on them. The system rotates at a constant rate with Coriolis parameter $f = 10^{-4} \text{ s}^{-1}$. Initially, the fluid is resting and uniformly stratified with a buoyancy frequency of $8.37 \times 10^{-4} \text{ s}^{-1}$.

Motion is induced by imposing a steady surface buoyancy loss that varies across the channel but is uniform along the channel. The forcing (in W m^{-2}) has the form

$$\mathcal{H}(y, z) = -400 \left\{ \tanh \left[\frac{2(y - 15 \text{ km})}{10 \text{ km}} \right] + 1 \right\} \delta(z), \quad (9)$$

where y is the cross-channel distance measured from the southern wall in km, and $\delta(z)$ is the Dirac delta function. This form of buoyancy loss tends to create a mixed layer frontal zone in the center of the channel. To the south, buoyancy loss is weak and a shallow convective layer grows, while to the north strong cooling rapidly generates a deep overturning layer. In order to allow convective cells to develop a small zero-mean, spatially white, random buoyancy loss is also applied for the first day of each integration. Forcing function (9) is unrealistic for the real ocean as its lateral gradient is uncharacteristic of air/sea fluxes. Nevertheless, real mid-latitude upper-ocean fronts are similar to our modelled front, although they are formed in different ways.

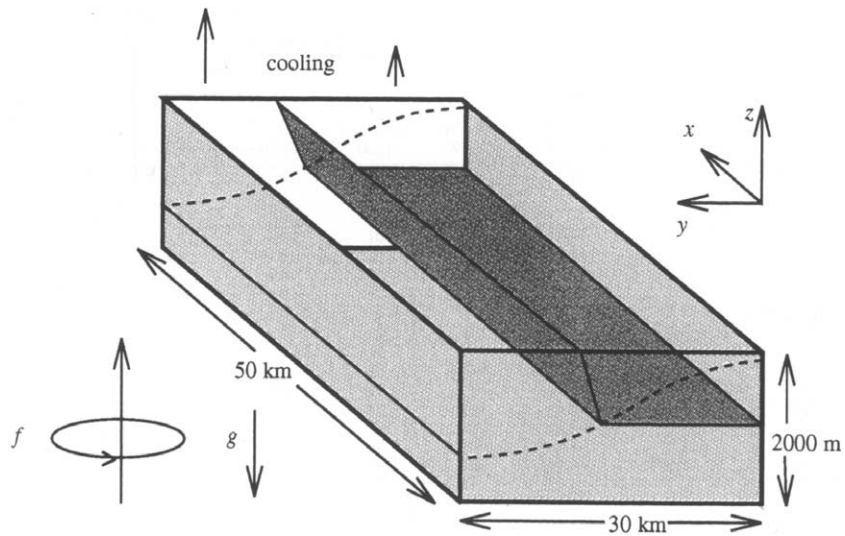


Fig. 1. Schematic diagram of the model configuration showing a surface front forming as a result of horizontally inhomogeneous surface buoyancy loss. Adapted from Haine and Marshall (1998).

The calculations are performed using the MIT general circulation model (Marshall et al., 1997a,b) on a massively parallel supercomputer. The horizontal grid spacing is 250 m with 20 vertical cells of thickness between 40 m at the surface and 400 m at the bottom. The explicit dissipation of momentum and heat are identical but anisotropic: $\nu_h = \kappa_h = 5 \text{ m}^2 \text{ s}^{-1}$ in the horizontal and $\nu_v = \kappa_v = 0.02 \text{ m}^2 \text{ s}^{-1}$ in the vertical direction. This dissipation guarantees numerical stability and coherent grid-scale vorticity without strongly affecting the resolved scales (see Section 3). We also simulate a passive scalar tracer (whose concentration satisfies an equation similar to (5)) with a surface source. The time-step is 60 s.

3. Results

As HM98 explain, the evolution of the flow in the channel follows three stages: First, the buoyancy loss causes gravitational instability on the northern side of the channel. Nonhydrostatic plumes drain the unstable, dense surface fluid and excavate a turbulent layer that deepens with time. There is little systematic variation in the flow along the channel, as expected from the uniform forcing in that direction. Second, after a few rotation periods, a baroclinic jet is induced by geostrophic adjustment of the surface front that is developing. Vigorous convection continues in the northern half of the channel. These motions may now be influenced by Coriolis forces – either by restriction of the horizontal scale of the sinking plumes (Jones and Marshall, 1993), or by slantwise overturning caused by symmetric instability (HM98). Again, there is no systematic along-channel variation on scales larger than the plume scale. The third stage involves the development of baroclinic waves along the mid-channel front. These waves grow to finite amplitude after a few days and then break producing a field of baroclinic vortices. These eddies now

dominate the flow. They provide a strong cross-channel heat flux allowing the front to slump. They also switch off the convection at mid-channel although rapid vertical overturning continues in the northern half.

The vertical velocity field early in the third stage of this development (day 6) is shown in Fig. 2(a). The rapid (several cm s^{-1}) up and down-welling plumes are clear in the northern half of the channel. Although these plumes are marginally resolved by our calculation, there is good agreement between their sinking speeds and inviscid scaling arguments (HM98). The ratio of up-welling to down-welling plume areas is around 2, also in good agreement with highly resolved calculations of nonhydrostatic convection (Kämpf and Backhaus, 1998). We infer that explicit dissipation in the model is not dominating the plume dynamics. At this time the convective plumes penetrate to a depth of around 1000 m. The baroclinic waves are less obvious in the vertical

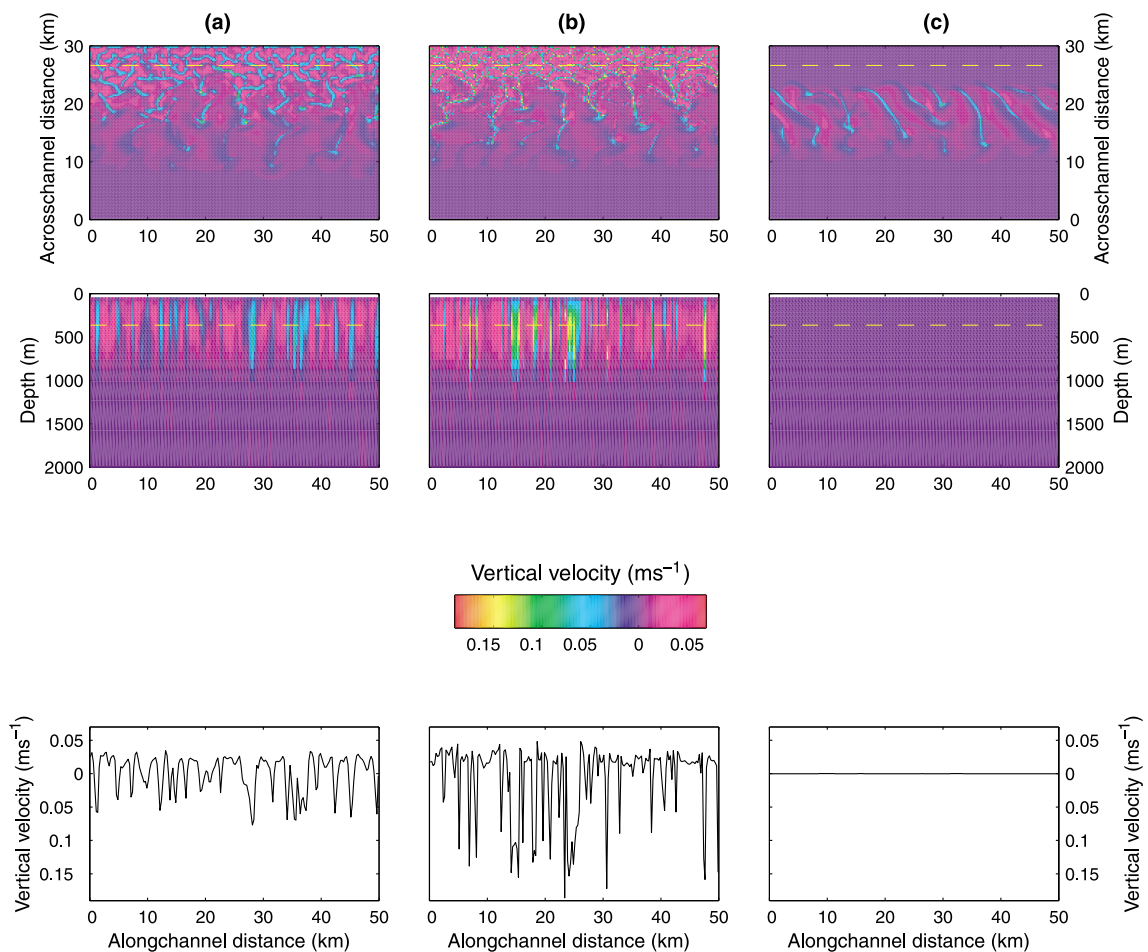


Fig. 2. Vertical velocity fields (m s^{-1}) after six days of integration in experiment: (a) NH, (b) HY, and (c) CA. In each case, the upper panel shows a horizontal section at 400 m depth, the middle panel shows a vertical section near the northern wall and the lower panel shows the vertical velocities at the intersection of these sections (the dashed line indicates this intersection). Modified from Marshall et al. (1997a) by permission of the American Geophysical Union.

velocity field but they dominate the flow at mid-channel near 400 m. At day 6 the waves are of finite amplitude but have not yet broken. The nonhydrostatic parameter $n = O(1)$ in the overturning layer of experiment NH confirming that vertical accelerations are important in the plume dynamics.

Figs. 2(b) and (c) show the same point in the integration of the hydrostatic (HY) and convective adjustment (CA) experiments. Interestingly, the hydrostatic model shows strong vertical overturning too. In this experiment the vertical speeds are excessive, however. The peak sinking plumes achieve speeds of 15 cm s^{-1} . They also occur on smaller horizontal scales – in fact, the overturning in the hydrostatic experiment is at the grid scale itself. In this experiment static instability is also being generated by the surface buoyancy loss. The model overturns to release the available potential energy but, because there is no inertia associated with vertical motion, its dynamics are wrong. The result is unrealistic convective plumes at the grid scale with excessive sinking speeds. Although our calculations are numerically stable it is possible that hydrostatic balance could lead to growing computational modes in some circumstances. In experiment CA (Fig. 2(c)) the overturning is dealt with by the convective adjustment parametrization itself. There are now no explicit plumes arising from gravitational instability. The vertical velocities that remain are due to convergence of the horizontal (nearly geostrophic) flow.

Clearly, the nonhydrostatic dynamics play a crucial role in the convective overturning. The vertical velocity field on scales up to $O(1 \text{ km})$ is strongly dependent on a proper treatment of the vertical momentum equation. But how important is it for the frontal evolution? We now address this question by examining the along-channel average temperature field (Section 3.1), tracer field (Section 3.2), and the water-mass formation rate (Section 3.3).

3.1. Average temperature and vertical overturning

Fig. 3 shows the along-channel-average temperature field at the end of day 9, for each of the three models. At this time the baroclinic eddies dominate the overall development of the flow. Near the southern wall (small y), the convective surface layer is shallow and the initial stratification is undisturbed. At the channel center the surface front is strongest with weakest vertical stratification near the northern wall. There are small, but significant, differences between the three experiments. (To judge their significance we show the result of a second nonhydrostatic calculation in Fig. 3(d). This experiment is identical to NH except it is in a channel of width and length 60 km. HM98 show that there is little systematic difference between these two NH integrations – they are comparable realizations of the same chaotic flow.) Compared to the nonhydrostatic solution, the hydrostatic model has a mid-channel front that is too surface-intensified and too strong on either side of mid-channel. Experiment HY does a reasonable job of producing well-mixed, but weakly stratified, fluid in the northern third of the channel. HM98 explain how symmetric instability along slanting paths resets (Ertel) potential vorticity to zero. This process leaves weak, but positive, stratification in the presence of lateral buoyancy gradients such as exist here. The implication is that slantwise overturning occurs in experiment HY (as well as NH), despite its defective vertical-force balance. The statistical distribution of stratification is very similar for both HY and CA (not shown). In the convective adjustment experiment the outcropping isotherms are too steep across the frontal zone. The fluid in the northern third of the

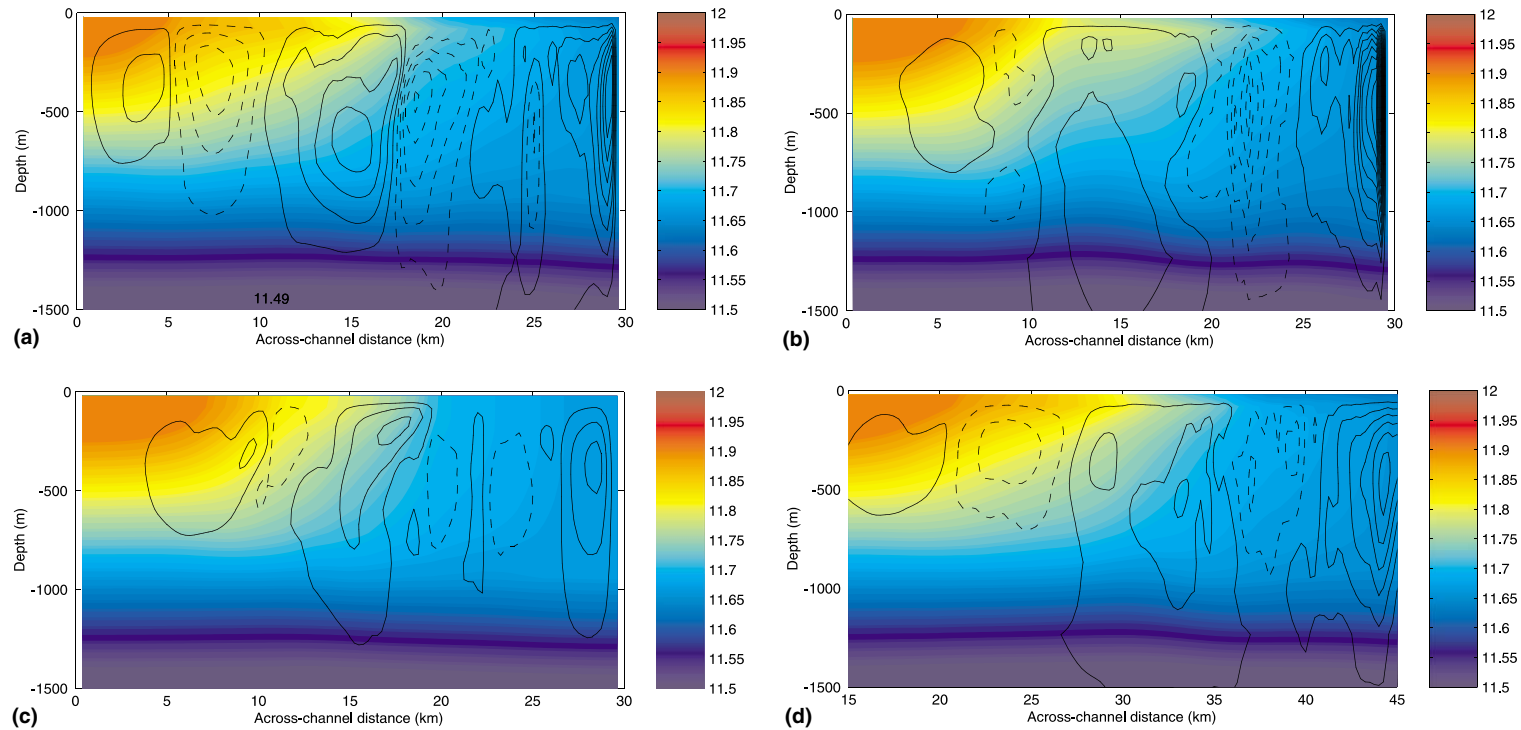


Fig. 3. Along-channel-average temperature ($^{\circ}\text{C}$) at day 9 from experiment: (a) NH, (b) HY, (c) CA, (d) wide-channel NH. The along-channel-average vertical overturning streamfunction is also shown (contour spacing $1 \text{ m}^2 \text{ s}^{-1}$ with clockwise circulation about positive (solid) streamlines). Only the upper 1500 m of the 2000 m deep channel are shown and the colour bars are drawn to match the initial stratification.

channel has vanishing vertical stratification in this case – symmetric instability has been suppressed by the convection scheme in experiment CA.

Fig. 3 also shows the overturning streamfunction for the along-channel-average circulation (contours). For each experiment, the clockwise overturning at mid-channel allows warm water to override cold water. This frontal slumping releases available potential energy and is accomplished by the baroclinic eddies (whose aspect ratio $\gamma \approx 1/6$). The magnitudes of these overturning motions are similar in each experiment although there are differences in the shapes of the cells (peak streamfunction of 2–4 $\text{m}^2 \text{s}^{-1}$ – results from other days suggest there is no systematic difference in strength of the mid-channel overturning between experiments). Interestingly, the hydrostatic experiment shows mid-channel overturning that is too deep, extending well below the convective layer. This flow must have been induced by inertia–gravity wave radiation from near the surface. Presumably, the excessively fast sinking plumes in experiment HY over-excite gravity waves when they plunge into the thermocline at the base of the convective layer. In the northern third of the channel the influence of the convective plumes is clear (overturning cells with $\gamma \approx 1$). Experiment HY has too rapid sinking while experiment CA has convection that is too weak (see this section above: the differences in sinking speeds are less in Fig. 3 than in Fig. 2 because the overturning streamfunction is an average through many ($O(100)$) plumes). Note that experiment CA shows vertical structure in the overturning streamfunction that is similar to NH. The convective adjustment algorithm removes vertical buoyancy anomalies but does not mix momentum. If it did so, presumably the CA mixed layer would look less like that in NH because the ageostrophic tilting mechanism of Nurser and Zhang (2000) could not stratify the upper levels. The baroclinic instability may also be adversely affected as it depends on the thermal wind there.

Comparison of the average temperature fields shows significant, although relatively minor, differences arising from our various treatments of the vertical force balance. Fig. 4 reveals a complementary view of the heat budget in these experiments. It shows a time series of the cumulative heat lost by the southern half of the channel for each experiment. This fluid volume loses heat by direct surface buoyancy loss (that is, due to \mathcal{H}) and also by (mainly) advective heat fluxes to the northern half of the channel. As explained above, the breaking baroclinic waves (days 6–9) support a large systematic cross-channel heat flux. The hydrostatic model overestimates the heat lost this way while the convective adjustment model underestimates it. But the differences between the three models, caused by the different vertical force balances, are small compared to the heat carried by the eddies themselves. They are also comparable to the difference between the 30 km-wide and 60 km-wide channel experiments. Indeed, the error in the eddy parametrization theory of HM98 exceeds these differences. In this sense, getting the convective (nonhydrostatic) dynamics right only makes $O(10\%)$ difference to the total heat transport across the front.

3.2. Average ventilation

Fig. 5 shows the along-channel-average tracer concentration field at the end of day 9, for each experiment. The passive tracer field directly reflects the ventilation, by surface contact, occurring in the flow. There is a strong correlation between tracer concentration and potential vorticity (not shown). This dependence is expected as both these fields are of conserved material properties with surface sources (see HM98 for details). The convective layer is clearly visible in the tracer field

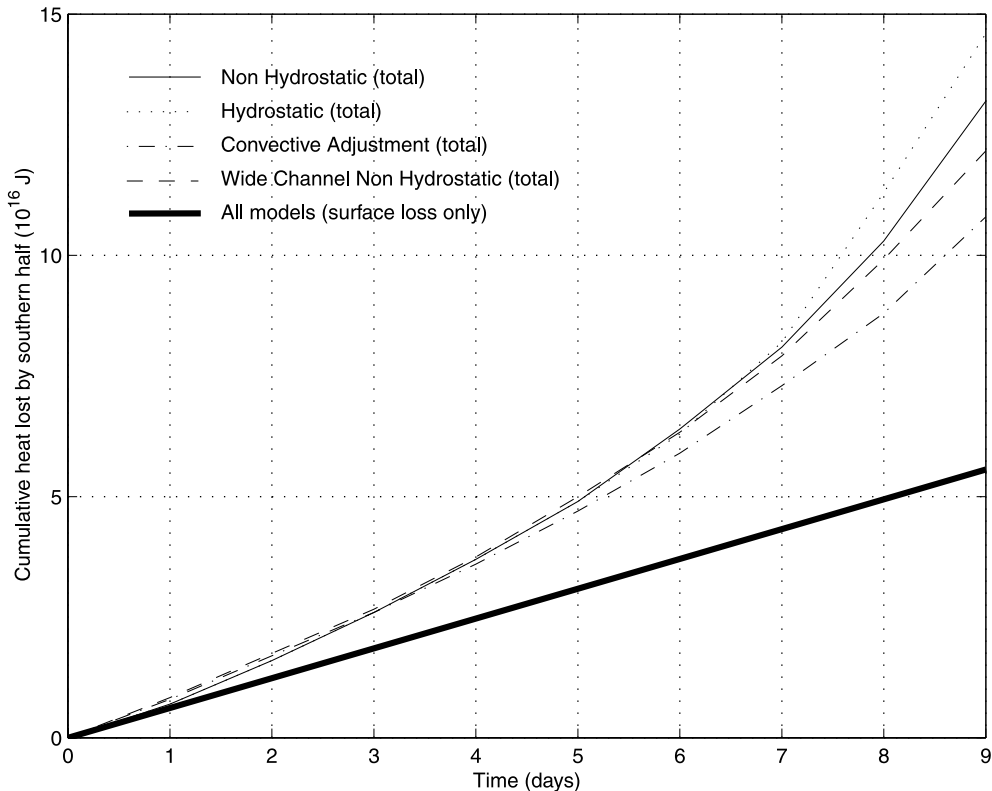


Fig. 4. Time series of cumulative heat lost (J) by the southern half of the channel since the start of the experiment for each simulation. Heat is lost by two processes: imposed surface loss (shown by the black line), and transport of heat to the northern half of the channel.

which also reveals the slumping process at mid-channel (warm, unventilated fluid overriding cold, ventilated fluid). Compared to the nonhydrostatic calculation, the hydrostatic experiment ventilates a layer that is too deep by about 10%. The convective adjustment experiment shows a transition from ventilated to unventilated fluid that is too sharp and slightly underestimates the depth of mixing in the southern half of the channel. A budget of the total mass of tracer substance in the southern half of the channel shows differences of only a few percent after 9 days (not shown). As for the average temperature and vertical overturning fields, experiment NH lies between experiments HY and CA but with just minor differences in average ventilation.

Note that the along-channel average tracer field in Fig. 5 evolves by advection due to the along-channel average flow (the overturning streamfunction) plus the effect of correlations between flow and tracer along the channel. One should not get the impression that the overturning cell is just smoothly carrying the average tracer field (as the coincidence of upwelling and the tracer plume near 10 km in Fig. 5(a) suggests). In fact, the streamfunction field varies in time and does not generally correspond to individual features in the average tracer field. The systematic effect of the overturning only becomes apparent when we look at the overall time evolution (as in Fig. 4, for example).

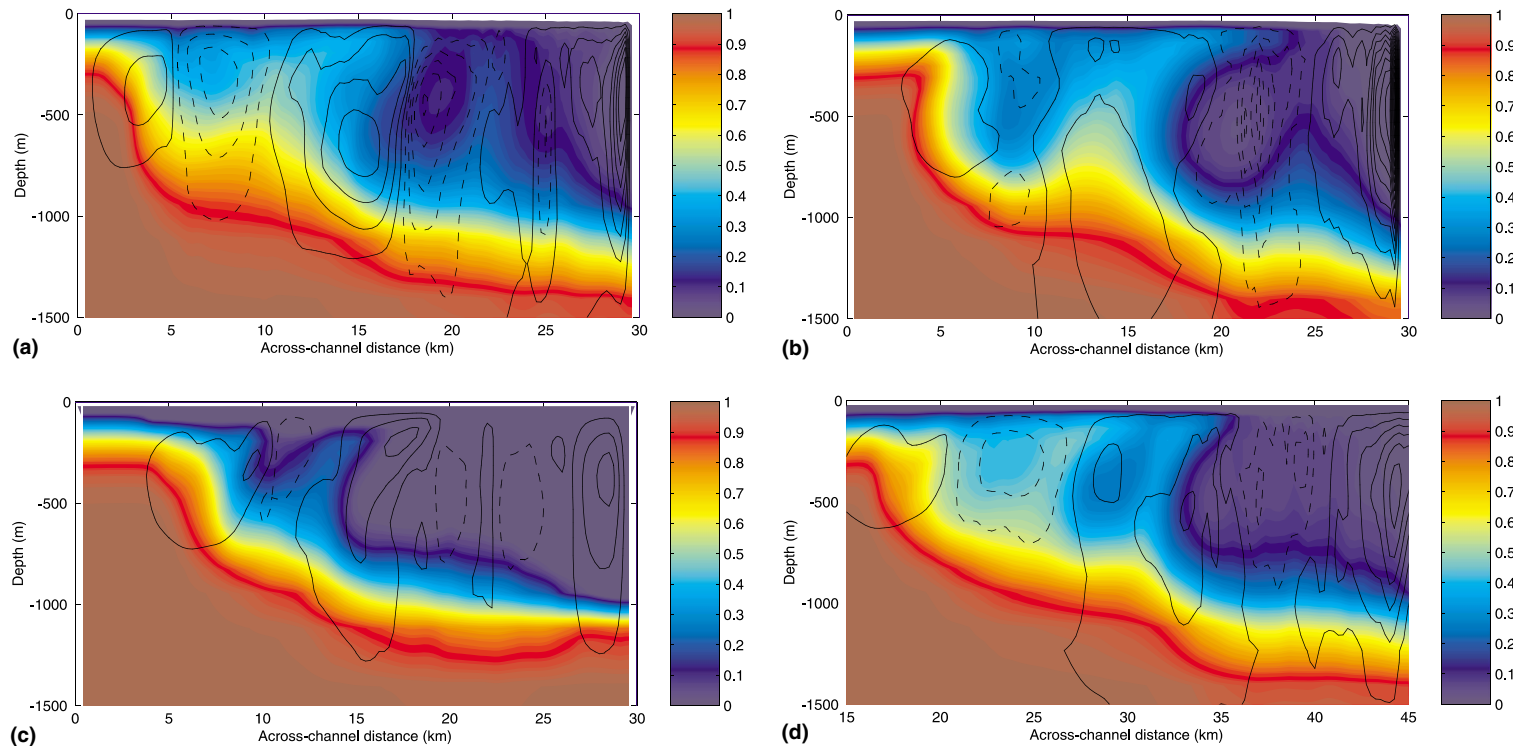


Fig. 5. Along-channel-average tracer concentration (arbitrary unit) at day 9 from experiment: (a) NH, (b) HY, (c) CA, (d) wide-channel NH. The only tracer source is the ocean surface. The along-channel-average vertical overturning streamfunction is also shown (contour spacing $1 \text{ m}^2 \text{ s}^{-1}$ with clockwise circulation about positive (solid) streamlines). Only the upper 1500 m of the 2000 m deep channel are shown.

3.3. Average water-mass formation

Finally, Fig. 6 shows the distribution of water-mass volume with temperature at day 9 and the water-mass formation rate at day 8.5 for each experiment. The distribution of water-mass volume with temperature (Fig. 6(a)) shows similar patterns for each experiment. All three experiments have formed a mode water with a temperature near $11.67\text{ }^{\circ}\text{C}$. Experiment CA is slightly ($0.02\text{ }^{\circ}\text{C}$) too warm with 15% too much water at that temperature. Experiment HY is $0.01\text{ }^{\circ}\text{C}$ too cold with 8% too little water. The differences between the three experiments are significant compared to the difference between the two nonhydrostatic calculations. Again, the nonhydrostatic solution lies between the HY and CA models.

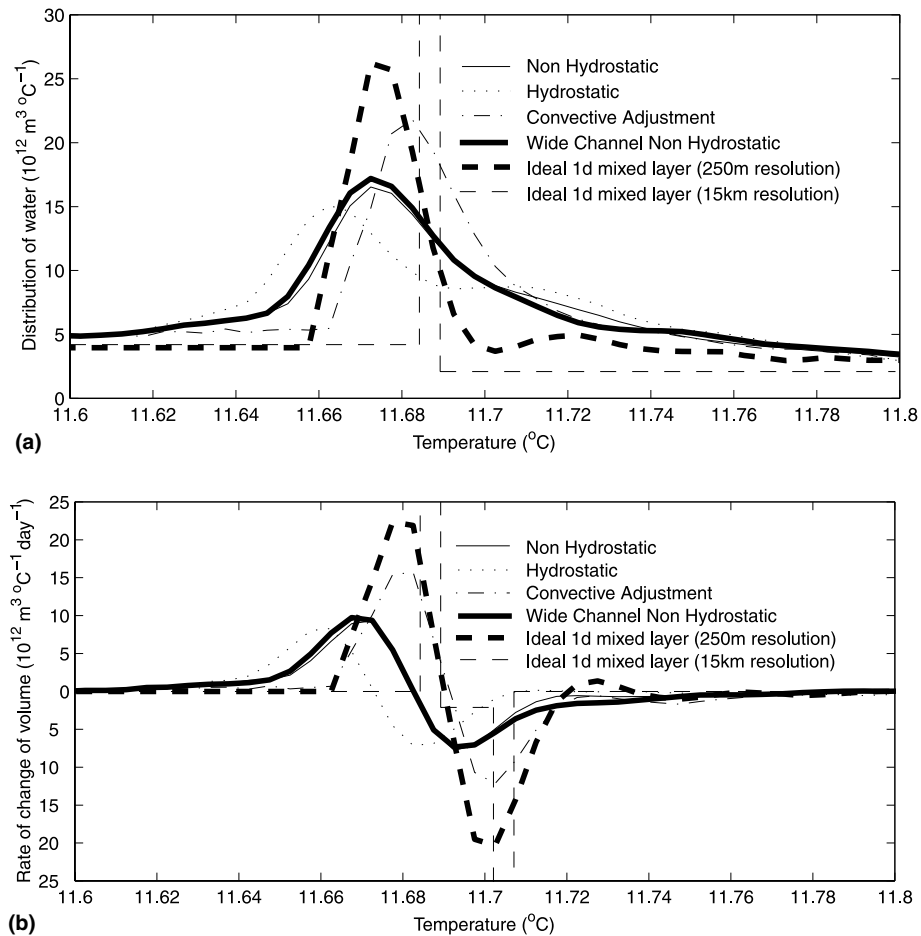


Fig. 6. (a) Water-mass temperature distribution ($\text{m}^3\text{ }^{\circ}\text{C}^{-1}$) at day 9 for each experiment. The prediction of an ideal one-dimensional theory is also shown for a horizontal grid resolution of 250 m and 15 km (see text). The result from the 15 km-resolution theory peaks offscale at $130 \times 10^{12}\text{ m}^3\text{ }^{\circ}\text{C}^{-1}$. The initial water-mass temperature distribution is uniform and equal to $4.5 \times 10^{12}\text{ m}^3\text{ }^{\circ}\text{C}^{-1}$. (b) Water-mass formation rate at day 8.5 ($\text{m}^3\text{ }^{\circ}\text{C}^{-1}\text{ day}^{-1}$). The result from the 15 km-resolution theory peaks offscale at $\pm 125 \times 10^{12}\text{ m}^3\text{ }^{\circ}\text{C}^{-1}\text{ day}^{-1}$.

The water-mass formation rate at day 8.5 is shown in Fig. 6(b). At this time the principal net conversion process is from water at 11.69 °C to water at 11.65 °C. Experiment CA overestimates this process by about 40% between water types that are around 0.1 °C too warm. Experiment HY accurately estimates the formation rates but for water that is about 0.1 °C too cool. Again these differences are significant with respect to the difference between the nonhydrostatic solutions.

In Fig. 6 we also show the water-mass properties predicted by an ideal one-dimensional convective adjustment algorithm with the same resolution as the full model. The ideal theory assumes no buoyancy transfer by eddies or diffusion. A simple buoyancy budget yields a mixed layer depth h at time t of

$$h = \sqrt{\frac{2\alpha g \mathcal{H}' t}{\rho_{\text{ref}} c N^2}}, \quad (10)$$

where N is the buoyancy frequency and \mathcal{H}' is the divergence of the heat source \mathcal{H} (that is, the surface heat loss itself: see also HM98). The theory predicts a water-mass distribution that is peaked at the right temperature but is too narrow (Fig. 6(a)). It therefore overestimates the mode-water distribution density by 70%. Baroclinic eddies cause the wider spread of water-masses in the numerical experiments (a simple scaling analysis implies that the explicit buoyancy diffusion is too weak to be important). For the water-mass formation rate (Fig. 6(b)) experiment CA is closer to the ideal theory than the nonhydrostatic solution at this time. The effect of the eddies on this diagnostic is smaller than the effect of the nonhydrostatic dynamics although they are similar. The result of applying this theory with a horizontal grid resolution of 15 km rather than 250 m is shown too. This case represents the result expected from an ocean GCM at about 1/6–1/8° resolution (neglecting horizontal fluxes). Now the ideal theory predicts a large volume of homogeneous water in the northern half of the channel. The water-mass distribution is strongly peaked at the temperature of this mode which is 0.02 °C too warm.

To accurately represent the water-mass distribution good resolution of the forcing function is needed. Real air/sea flux fields do not contain gradients as strong as that used in our experiments, however. In this sense, our comparison is rather extreme and likely to emphasize the differences between different treatments of the vertical momentum balance. Although nonhydrostatic effects are significant the baroclinic eddies are more important in general. So, the principal benefit of refining a GCM resolution from 15 km would be to better resolve gradients in the forcing fluxes and to better represent the O(1 km) near-geostrophic scales rather than the nonhydrostatic effects.

4. Discussion

In this paper we have examined the effect of nonhydrostatic dynamics on cross-frontal exchange and development where the front is generated by deep convection. Nonhydrostatic dynamics control the vertical velocity field associated with the convective plumes on scales up to about 1 km. The calculation using hydrostatic balance substantially overestimates the vertical sinking speed in plumes that are too narrow (on the model grid-scale). Use of a convective-adjustment scheme removes all plume-scale convection to leave a feeble vertical velocity field associated with horizontal divergence of the geostrophic flow. But when we examine average frontal development in our experiments, and the overall water-mass conversion process, the

typical effect of nonhydrostatic dynamics is minor. The calculation with hydrostatic balance tends to produce slightly too much mixing and slightly overestimates the depth of the mixed layer. Convective adjustment slightly underestimates the cross-frontal eddy heat flux and produces a mode water that is a little too homogeneous and warm. In each of the diagnostics we have studied, the nonhydrostatic model (taken to represent the true dynamics) lies between the hydrostatic and convective-adjustment solutions. These differences are significant compared to the typical difference between two nonhydrostatic realizations. For the case of cross-frontal heat flux the differences are smaller than the flux carried by the nearly geostrophic and hydrostatic baroclinic eddies. Averaged over horizontal scales of $O(10\text{ km})$, nonhydrostatic dynamics have little net effect on cross-frontal exchange. For the case of water-mass distribution and formation rate the relative importance of baroclinic eddies and nonhydrostatic dynamics are similar although resolving the gradients in forcing fluxes is more critical. Overall, the impact of nonhydrostatic dynamics is largely restricted to scales of less than 1 km, at least in these experiments on convectively driven mid-latitude ocean fronts.

These results support the findings of HM98. In this earlier paper we suggested that the net effect of gravitational and symmetric instability is to generate a pool of stirred fluid that has its potential vorticity reset to near zero. The subsequent baroclinic instability seems to be insensitive to the details of these convective dynamics occurring on scales 1 decade shorter. The front itself is formed by nonhydrostatic processes and the surface buoyancy loss persists throughout the integration. But a near-geostrophic, and hydrostatic, flow quickly adjusts and then undergoes a baroclinic instability that is largely independent of the convective forcing. Such a loose coupling of the slow (vortical) and fast (inertia-gravity) motions bodes well for the applicability of a convective-adjustment-type parametrization. But, in these calculations with a surface front, the state of zero potential vorticity does not correspond to a state of vanishing vertical stratification. Rather, there is a positive vertical stratification associated with the front's thermal wind shear. The appropriate adjustment algorithm should thus remove gravitational and symmetric instabilities to yield a state of zero potential vorticity. Such a parametrization may well give better agreement with the nonhydrostatic solutions here. In this sense we have set a more stringent test than the work of Klinger et al. (1996) on plume parametrization in open-ocean deep convection. They studied an unstratified, or weakly stratified, fluid where symmetric overturning is less important. Our results confirm and extend their findings to surface ocean fronts.

These calculations focus on the transition between nonhydrostatic plume dynamics and hydrostatic, geostrophic flow. To do so with limited computational resources we have omitted several effects that are important in the real ocean. In particular, our grid resolution is only marginally capable of representing nonhydrostatic plumes. Accurate plume dynamics may need grid spacing of $O(10\text{ m})$ (Kämpf and Backhaus, 1998). It is possible, therefore, that the uncaptured plume interactions on scales of $O(100\text{ m})$ might be significant for the scales of $O(1\text{--}10\text{ km})$. Higher resolution calculations are needed to confirm the results here. For convenience, we have also neglected the influence of other dynamical processes relevant to real ocean fronts. These include thermobaric effects and double-diffusive mixing which arise from an accurate equation of state for seawater. Also, real ocean mixed layers and surface fronts are driven by more complicated air/sea/ice interaction. Marshall and Schott (1999) and The Lab Sea Group (1998) provide helpful recent reviews. In any event, the processes we study here are likely to be important in general even if other mechanisms also contribute.

The implication of this study for ocean GCMs is that hydrostatic balance and convective adjustment are likely to give accurate solutions on scales down to $O(1\text{ km})$. As resolution is further refined, without nonhydrostatic effects, the convective dynamics will be misrepresented but the flow on scales $O(1\text{ km})$ and larger will be reasonably well-captured. The key challenge facing GCM builders now is to resolve these short baroclinic scales which mediate the cross-frontal exchange shown here. Including these motions may make a profound difference to the simulation of fronts and their mixing. In contrast, the benefit of including a prognostic vertical momentum equation is unlikely to be so great.

Acknowledgements

Discussions with Amala Madahevan, John Marshall, and Martina Junge were helpful. This study is based on PDW's M.Phys. undergraduate project at the Department of Physics, University of Oxford.

References

- Cox, M.D., 1984. A primitive equation, 3-dimensional model of the ocean. Technical Report, GFDL Ocean Group Technical Report No. 1. Geophysical Fluid Dynamics Laboratory, P.O. Box 308, Princeton, NJ, 08542.
- Haine, T.W.N., Marshall, J.C., 1998. Gravitational, symmetric and baroclinic instability of the ocean mixed layer. *J. Phys. Oceanogr.* 28, 634–658.
- Jones, H., Marshall, J., 1993. Convection with rotation in a neutral ocean: a study of open-ocean deep convection. *J. Phys. Oceanogr.* 23, 1009–1039.
- Kämpf, J., Backhaus, J.O., 1998. Shallow, brine-driven free convection in polar oceans: nonhydrostatic numerical process studies. *J. Geophys. Res.* 103, 5577–5593.
- Klinger, B., Marshall, J., Send, U., 1996. Representation of convective plumes by vertical adjustment. *J. Geophys. Res.* 101, 18175–18182.
- Marotzke, J., 1991. Influence of convective adjustment on the stability of the thermohaline circulation. *J. Phys. Oceanogr.* 21, 903–907.
- Marshall, J., Schott, F., 1999. Open-ocean convection: observations, theory and models. *Rev. Geophys.* 37, 1–64.
- Marshall, J., Adcroft, A., Hill, C., Perelman, L., Heisey, C., 1997a. A finite-volume, incompressible Navier–Stokes model for studies of the ocean on parallel computers. *J. Geophys. Res.* 102, 5753–5766.
- Marshall, J., Hill, C., Perelman, L., Adcroft, A., 1997b. Hydrostatic, quasi-hydrostatic, and non-hydrostatic ocean modeling. *J. Geophys. Res.* 102, 5733–5752.
- Nurser, A.J.G., Zhang, J.W., 2000. Eddy-induced mixed layer shallowing and mixed layer/thermocline exchange. *J. Geophys. Res.* 105, 21851–21868.
- The Lab Sea Group, 1998. The Labrador Sea deep convection experiment. *Bull. Am. Meteor. Soc.* 79, 2033–2058.